Eye-specific 3D modeling of factors influencing oxygen concentration in the lamina cribrosa

Yi Hua,[1†] Yuankai Lu,[1†] Jason Walker,[2†] Po-Yi Lee,[1,3] Qi Tian,[1,3] Haiden McDonald,[2] Pedro Pallares,[2] Fengting Ji,[1,3] Bryn L. Brazile,[1] Bin Yang,[1,4] Andrew P. Voorhees,[1] Ian A. Sigal[1,3] *

[†] Authors contributed equally to the manuscript

[1] Department of Ophthalmology, University of Pittsburgh, Pittsburgh, Pennsylvania, United States
[2] Department of Biological Science, University of Pittsburgh, Pittsburgh, Pennsylvania, United States
[3] Department of Bioengineering, University of Pittsburgh, Pittsburgh, Pennsylvania, United States
[4] Department of Engineering, Rangos School of Health Sciences, Duquesne University, Pittsburgh, Pennsylvania, United States

Short title: LC hemodynamics and oxygenation

*** Correspondence:**
Ian A. Sigal, Ph.D.
Laboratory of Ocular Biomechanics
Department of Ophthalmology, University of Pittsburgh School of Medicine
203 Lothrop Street, Eye and Ear Institute, Rm. 930, Pittsburgh, PA 15213
Phone: (412) 864-2220; Fax: (412) 647-5880
Email: ian@OcularBiomechanics.com
www.OcularBiomechanics.com

Keywords: glaucoma, lamina cribrosa, vasculature, hemodynamics, oxygen, blood flow

Conflict of Interest: Y. Hua, None; Y. Lu, None; J. Walker, None; P.Y. Lee, None; Q. Tian, None; H. McDonald, None; P. Pallares, None; F. Ji, None; B.L. Brazile was at the University of Pittsburgh when he contributed to this work. He is now at Baxter; B. Yang, None; A.P. Voorhees was at the University of Pittsburgh when he contributed to this work. He is now at Johnson & Johnson; I.A. Sigal, None.

Funding: Supported by National Institutes of Health R01-EY023966, R01-EY028662, R01-EY031708, P30-EY008098, R01-HD045590, R01-HD083383, and T32-EY017271; Eye and Ear Foundation (Pittsburgh, Pennsylvania), Research to Prevent Blindness and Brightfocus Foundation.

Accepted by Experimental Eye Research on April 28th 2022

Abstract

Our goal was to identify the factors with the strongest influence on the minimum lamina cribrosa (LC) oxygen concentration as potentially indicative of conditions increasing hypoxia risk. Because direct measurement of LC hemodynamics and oxygenation is not yet possible, we developed 3D eye-specific LC vasculature models. The vasculature of a normal monkey eye was perfusion-labeled post-mortem. Serial cryosections through the optic nerve head were imaged using fluorescence and polarized light microscopy to visualize the vasculature and collagen, respectively. The vasculature within a 450 µm-thick region containing the LC – identified from the collagen, was segmented, skeletonized, and meshed for simulations. Using Monte Carlo sampling, 200 vascular network models were generated with varying vessel diameter, neural tissue oxygen consumption rate, inflow hematocrit, and blood pressures (arteriole, venule, pre-laminar, and retro-laminar). Factors were varied over ranges of baseline ±20% with uniform probability. For each model we first obtained the blood flow, and from this the neural tissue oxygen concentration. ANOVA was used to identify the factors with the strongest influence on the minimum (10th percentile) oxygen concentration in the LC. The three most influential factors were, in ranked order, vessel diameter, neural tissue oxygen consumption rate, and arteriole pressure. There was a strong interaction between vessel diameter and arteriole pressure whereby the impact of one factor was larger when the other factor was small. Our results show that, for the eye analyzed, conditions that reduce vessel diameter, such as vessel compression due to elevated intraocular pressure or gaze-induced tissue deformation, may particularly contribute to decreased LC oxygen concentration. More eyes must be analyzed before generalizing.

1. Introduction

The optic nerve head (ONH) is a site of initial retinal ganglion cell damage in glaucoma. (Quigley and Anderson, 1976; Quigley et al., 1995) In particular, glaucomatous damage is believed to initiate within the lamina cribrosa (LC) region of the ONH. The LC is a highly vascular structure in which vessels form a complex network, intertwined with collagen beams, that provides nutritional and oxygen support to retinal ganglion cell axons. (Brazile et al., 2020; Hayreh, 1996; Levitzky and Henkind, 1969) The causes for retinal ganglion cell axon damage occurring within the LC early are not yet understood. (Burgoyne et al., 2005; Chuangsuwanich et al., 2016; Chuangsuwanich et al., 2020; Sigal and Ethier, 2009; Sigal et al., 2007; Sigal and Grimm, 2012; Voorhees et al., 2020; Zhang et al., 2015) One of the leading hypotheses postulates that insufficient nutrient and oxygen supply within the LC cause or contribute to retinal ganglion cell axon damage. (Stefánsson et al., 2005) This can happen at any level of intraocular pressure (IOP), and is likely to worsen if elevated IOP induces LC deformations that distort the vasculature and compromise blood flow. (Burgoyne et al., 2005; Fechtner and Weinreb, 1994; Quigley et al., 2000) Predicting susceptibility to retinal ganglion cell damage and vision loss, at all levels of IOP, thus requires a comprehensive understanding of the characteristics (*e.g.*, LC capillary diameters) and conditions (*e.g.*, blood perfusion pressure) that determine the LC hemodynamics and oxygenation, and most importantly, the risk of regions of low oxygenation.

Unfortunately, experimental measurements of LC blood flow and oxygenation are not yet possible, and alternate approaches are therefore needed. One such approach is modeling. Several mathematical models have been developed. (Carichino et al., 2012; Causin et al., 2014) These models, while insightful, the challenges of the analytical approach required the authors to assume a highly simplified LC vasculature, and thus the models have limited ability to predict conditions in specific eyes. More recently, models using computational fluid dynamics have incorporated more complex vessels. (Chuangsuwanich et al., 2016; Chuangsuwanich et al., 2020) Nevertheless, the vascular network in these models was still substantially simplified. The models were generic, *i.e.*, not specific to an eye, and did not incorporate the full 3D vascular network. In addition, the analysis of factor influences of these studies did not account for possible interactions between factors. Assessing eye-specific hemodynamics and LC oxygenation of a specific eye will benefit from models that incorporate the complex 3D vascular network of the eye, including interactions.

Our goal in this study was to identify the factors with the strongest influence on the LC oxygenation in a specific eye. To achieve this goal, we developed a novel eye-specific 3D model

of the LC vascular network, which we use to predict LC hemodynamics. From the hemodynamics, we then used a diffusion-consumption model to predict the oxygenation throughout the LC. Specifically, we focused our analysis on the factor influences on the minimum (10th percentile) oxygen concentration as potentially indicative of conditions relevant to hypoxia. We used a Monte Carlo approach to generate a series of models, which we then analyzed to identify the factors that most influence the minimum oxygen concentration in the LC.

2. Methods

General procedure. The vasculature of a normal monkey ONH was labeled, imaged, and reconstructed following the process described elsewhere. (Lee et al., 2021; Waxman et al., 2021) From the 3D vessel reconstructions we created a large set of vascular network models with varying vessel diameter, neural tissue oxygen consumption rate, pressures (arteriole, venule, pre-laminar, and retro-laminar), and inflow hematocrit. Blood flow and neural tissue oxygen concentration were then, in turn, estimated using algorithms described elsewhere. (Secomb et al., 2004) ANOVA was used to identify the factors with the strongest influence on the minimum (10th percentile) oxygen concentration in the LC. The steps are described in detail below.

2.1 Reconstruction of a 3D eye-specific LC vascular network

All procedures were approved by the University of Pittsburgh's Institutional Animal Care and Use Committee (IACUC), and adhered to both the guidelines set forth in the National Institute of Health's Guide for the Care and Use of Laboratory Animals and the Association of Research in Vision and Ophthalmology (ARVO) statement for the use of animals in ophthalmic and vision research.

Vessel labeling. The head and neck of a healthy 15-year-old female rhesus macaque monkey were received within 30 minutes of sacrifice. The anterior chamber of each eye was cannulated to control IOP using a saline fluid column (**Figure 1a**). IOP was set to 5 mmHg throughout the experiment to avoid hypotony or hypertension. Two polyimide micro-catheters (Doccol Inc., Sharon, MA) were inserted into the carotid arteries on each side of the neck. The vascular bed was washed with warm phosphate-buffered saline (PBS) to remove intravascular blood. To avoid vessel damage, the PBS perfusion was minimal at first, and then progressively increased over several minutes as the output solution cleared, indicating blood washout. The PBS wash continued for at least 10 minutes after the output was clear. DiI, a lipophilic carbocyanine dye, was used to label the vessels in the eye. (Li et al., 2008) We perfused 100 mL of aqueous DiI solution into each carotid artery at a rate of 5-10 mL/min for 10 minutes, followed by a PBS wash

to remove residual DiI. We then perfused 50 mL of 10% formalin into each carotid artery twice, with an interval of 15 minutes. After an additional 15 minutes, both eyes were enucleated, making sure to preserve optic nerves at least 10 mm in length from the globe. The IOP control lines were switched from saline to 10% formalin columns. To complete the fixation, both eyes were immersion fixed overnight in 10% formalin while IOP was maintained at 5 mmHg.

Histology and imaging. The right eye was hemisected, and the retina was examined under a dissecting fluorescence microscope (Olympus MVX10, Olympus, Tokyo, Japan) to evaluate vessel labeling. The image showed continuous staining of the retinal vasculature without any discernible dark patches or leaks, suggesting that the eye had satisfactory perfusions. The details of the process to confirm complete perfusion of the ONH vasculature are described and discussed elsewhere. (Lee et al., 2021; Waxman et al., 2021) The most important of these are also addressed in the Discussion of this manuscript. The ONH and surrounding sclera were isolated using a 14-mm-diameter circular trephine. The tissues were placed in 30% sucrose overnight for cryoprotection, flash-frozen in optimum cutting temperature compound (Tissue Plus, Fisher Healthcare, Houston, TX), and sectioned coronally at 16 µm thickness with a cryostat (Leica CM3050S). Immediately after sectioning, the sections were hydrated and cover-slipped for imaging. Both fluorescence microscopy (FM) and polarized light microscopy (PLM) images were acquired of each section using a commercial inverted microscope (IX83, Olympus, Tokyo, Japan) to visualize the vessels and collagen, respectively (**Figure 1b**). (Brazile et al., 2020; Jan et al., 2015) Image acquisition was controlled using Olympus CellSens software.

3D vasculature reconstruction. Stacks of sequential FM and PLM images were imported and registered based on the collagen in Avizo (version 9.1, FEI; Thermo Fisher Scientific). The transformations necessary for registering the collagen were then applied to the vessel images. The vessels were segmented using a semi-automated algorithm based on a Hessian filter. (Jerman et al., 2016) The vessel segmentations or “labels” were combined to create a 3D map of the vasculature (**Figure 1c**). We identified the vessels in the LC region based on the presence of collagen beams. (Brazile et al., 2018; Jan et al., 2017a; Jan et al., 2017b; Voorhees et al., 2020; Voorhees et al., 2017a; Voorhees et al., 2017b) Overall, we reconstructed the vessels within the scleral canal, “feeder” vessels in the periphery, and some pre-laminar and retro-laminar regions. This ensured that the 3D LC network was fully enclosed within the region reconstructed, without any of the LC vessels directly in the model boundary. The 3D vasculature was skeletonized and converted into a graph in which all vessels were connected except at the periphery. During the skeletonization, we assumed the cross section of vessels to be circular, and kept the curvature of the vessel centerline. The skeleton was then converted into a mesh for solving flow numerically.

Convergence tests were performed, and adequate accuracy (relative differences in the maximum blood flow rate under 3%) was achieved with a mesh consisting of 14,448 elements and 10,571 nodes. Based on the literature, (An et al., 2021) we assumed that all capillaries have the same uniform diameter of 8 µm.

2.2 Pressure conditions

The model boundaries were divided into four regions for assigning the blood pressure conditions that drive the blood flow throughout the vascular network (Figure 2). We first selected baseline values for each blood pressure boundary. Then, to fairly compare their effects when analyzing the relative factor influences, all boundary blood pressures were varied by ±20% from their baseline values. This is important as it implies that we are comparing factor influences in an unbiased way that assumes the same range of variation. This is helpful to understand the fundamental role that each factor has on the system. Other factor levels and ranges may be necessary if the goal is to understand the potential roles of pathology, for example. A thorough discussion of this is beyond the scope of this work. Interested readers may consult the literature (Hua et al., 2017; Hua et al., 2018; Voorhees et al., 2016; Voorhees et al., 2018) Below we describe our rationale for choosing the baseline values. Further considerations of the rationale and impact of our choices are addressed in the Discussion.

At the periphery and center: For the boundary conditions at the periphery and center we followed the precedent established by previous studies modeling LC blood flow. (Chuangsuwanich et al., 2016; Chuangsuwanich et al., 2020; Mozaffarieh et al., 2014) Specifically:

> **At the periphery:** An arteriole pressure of 50 mmHg was set as baseline to represent blood inflow from the circle of Zinn-Haller. (Chuangsuwanich et al., 2016; Chuangsuwanich et al., 2020)
>
> **At the center:** A venule pressure of 15 mmHg was set as baseline to represent blood drainage through the central retinal vein. (Chuangsuwanich et al., 2016; Chuangsuwanich et al., 2020; Mozaffarieh et al., 2014)

At the anterior and posterior model boundaries: To the best of our knowledge, no model of LC hemodynamics had accounted for the detailed vascular interconnections between regions that are considered in our model, and thus there was no precedent to follow. We assumed that under normal conditions the capillaries at the anterior and posterior boundaries do not collapse. Because the capillary wall is very thin, i.e., mostly consisting of a single layer of endothelial cells,

this meant that the blood pressure in the capillaries should be at least as high as the surrounding tissue pressure. We could then use tissue pressures to estimate the worst-case blood pressures.

At the anterior boundary: The tissues of the pre-laminar region are primarily neural and glial, and thus highly compliant. Because the tissues cannot bear substantial loads, the pressure decrease across them is minimal, which we will approximate by zero. This, in turn, means that we could assume that the tissue pressure at the anterior model boundary was equal to IOP. This is consistent with experimental observations using micropipettes in the beagle dog ONH of Morgan and colleagues. (Morgan et al., 1998) It is also common for numerical models of the LC that do not explicitly account for pre-laminar tissues to assume the tissue pressures at the anterior LC surface to be equal to IOP (Roberts et al., 2010). Hence, we assigned a baseline blood pressure of 20 mmHg to the anterior boundary vessels. A baseline value of 20 mmHg results in an anterior boundary blood pressure range from 16 mmHg to 24 mmHg. Note that even though this pressure was estimated from IOP, its range is only intended to explore the relative influence of the parameter. This range is not intended to simulate the effects of IOP variations or of the effects of highly elevated IOP as may be related to pathology, for instance to assess susceptibility to glaucoma.

At the posterior boundary: For the tissue pressure at the posterior boundary, the situation is more complex as the pressure directly behind the LC is believed to be related to, but not identical to the cerebrospinal fluid pressure (CSFP). The experiments from Morgan and colleagues suggest that retro-laminar tissue pressure can be approximated by 0.82 × CSFP + 2.9 mmHg. (Morgan et al., 1998) Following a similar approach as for the anterior boundary, we could estimate a minimum blood pressure such that under normal conditions the capillary blood pressure is no lower than tissue pressure, preventing the capillaries from collapsing. Assuming an estimated CSFP of 16 mmHg, (Feola et al., 2016; Hua et al., 2018) we can derive baseline posterior boundary blood vessel pressure of 16 mmHg, with a range for factor influence analysis between 12.8 mmHg and 19.2 mmHg. As for IOP, the values of the blood pressures were estimated from CSFP, but they are not intended to represent variations in CSFP and how this pressure may affect susceptibility to disease.

Another consideration for our model is that the region reconstructed and simulated was larger than the LC. This means that there was a “buffer” region between the prescribed boundaries and the LC of interest.

2.3 Modeling blood flow within vessels

The behavior of blood flow in single vessels was assumed to follow Poiseuille's Law

$$Q = \frac{\pi}{128} \cdot \frac{d^4}{l} \cdot \frac{1}{\eta} \cdot \Delta p \tag{1}$$

where Q is the volume flow rate (nL/min), d the vessel diameter (m), l the vessel length, η the blood viscosity (Pa·s), and Δp the pressure drop along the vessel. The blood viscosity η was described as a function of vessel diameter and hematocrit (*i.e.*, the volume fraction of red blood cells). (Pries et al., 1994; Pries and Secomb, 2005) The Reynolds number for blood flow in capillaries is very low, indicating that the blood is flowing in a smooth and laminar fashion. In this sense, the cross-sectional velocity profile of a curved vessel would be similar to that of a straight circular cylinder. (Pries et al., 1994; Wang and Bassingthwaighte, 2003) Therefore, the Poiseuille law can still provide a reasonable approximation of the blood flow in tortuous vessels in our study.

Following the work of Pries and Secomb, (Pries and Secomb, 2008) we specified the hematocrit at all inflow boundary vessels as 0.45. The hematocrit at the outflow vessels was determined by the solver. The partition of hematocrit at vessel bifurcations was described by a function of flow rates, vessel diameters, and hematocrit of parent vessels. (Pries et al., 1989; Pries and Secomb, 2005)

2.4 Modeling oxygen concentration in neural tissues

We employed a Green's function method to estimate oxygen concentration in neural tissues. (Secomb et al., 2004) This method has been used to simulate oxygen transport from microvascular networks to tissues in skeletal muscle, (Hsu and Secomb, 1989; Secomb and Hsu, 1994) tumors, (Secomb et al., 1998; Secomb et al., 1993) brain, (Secomb et al., 2000) and LC (Chuangsuwanich et al., 2020). The essential idea of the Green's function method is to represent vessels as a set of discrete oxygen sources, and tissues as oxygen sinks embedded regularly throughout the vascular network. In this study, the density of neural tissue points (*i.e.*, oxygen sinks) was fixed at 6,500 points/mm^3, consistent with previous studies modeling the LC. (Chuangsuwanich et al., 2020) The modeled region thus contained 14,680 oxygen-consuming neural tissue points. The tissue region was considered as embedded in an effectively infinite domain with the same diffusivity, without oxygen sources or sinks outside the specified tissue region. (Groebe, 1990)

The governing equations for the Green's function method are detailed in (Secomb et al., 2004). Briefly, the oxygen diffusion in neural tissues was described by Fick's law

$$D\alpha\nabla^2 P = M\left(P\right) \tag{2}$$

where D is the oxygen diffusion coefficient of neural tissues ($cm^3O_2\ cm^{-1}\ s^{-1}\ mmHg^{-1}$), α is the oxygen solubility coefficient of neural tissues ($cm^3O_2/cm^3/mmHg$), ∇^2 is the Laplacian operator, P is the oxygen concentration in neural tissues (mmHg), and $M\left(P\right)$ is the oxygen consumption rate of neural tissues that can be estimated by

$$M(\mathrm{P}) = \frac{M_0 P}{P_0 + P} \tag{3}$$

where M_0 is the maximum oxygen consumption rate ($cm^3O_2\ (100\ cm^3)^{-1}\ min^{-1}$), and P_0 is the Michaelis-Menten constant corresponding to the oxygen concentration at half-maximal consumption. In this study, M_0 was assumed to be uniform throughout the LC.

The rate of oxygen transport along a vessel segment was given by

$$f\left(P_b\right) = Q\left(H_D C_0 S\left(P_b\right) + \alpha_{eff} P_b\right) \tag{4}$$

where H_D is the hematocrit, C_0 is the concentration of hemoglobin-bound oxygen in a fully saturated red blood cell (cm^3O_2/cm^3), P_b is the blood oxygen concentration (mmHg), $S\left(P_b\right)$ is the oxygen-hemoglobin saturation as determined by Hill equation, (Hill, 1921) and α_{eff} is the effective solubility of oxygen in blood ($cm^3O_2/cm^3/mmHg$).

Conservation of oxygen implied that

$$\frac{df\left(P_b\right)}{ds} = -q_v\left(s\right) \tag{5}$$

in each vessel segment, where s is the distance along the vessel segment (m), and $q_v\left(s\right)$ is the rate of diffusive oxygen efflux per unit vessel length.

At the interface between blood vessel and tissue, the diffusive oxygen flux across the interface and the oxygen concentration must be continuous, implying that

$$q_v\left(s\right) = -D\alpha\int_0^{2\pi} \frac{\partial P}{\partial r} r_v d\theta \tag{6}$$

where r is the radial distance from the vessel centerline (m), r_v is the vessel radius (m), and the integral is around the circumference, denoted by angle θ.

A list of constants used in the Green's function method is provided in **Table 1**.

2.5 Parametric analysis of factor influences

The model was parameterized to allow independent and simultaneous variations in seven factors: vessel diameter, neural tissue oxygen consumption rate, pressures (arteriole, venule, pre-laminar, and retro-laminar), and inflow hematocrit. These factors were chosen as they may affect the blood flow and oxygen concentration in the LC based on our understanding and previous findings of LC hemodynamics. (Chuangsuwanich et al., 2016; Chuangsuwanich et al., 2020) Factor baseline values were obtained from the literature (**Table 2**). The range of these factors remains unknown. To assess their relative influence in an unbiased manner we varied them by the same ±20% from their baseline values.

Using Monte Carlo sampling, we created 200 models. (Montgomery, 2017) The factor configurations formed an orthogonal array, which means that all factors were sampled in a balanced manner. The correlation coefficient between any two factors was less than 0.02. We randomized the order in which the factor configurations were pre-processed, simulated, and analyzed.

As model responses, we focused on the minimum oxygen concentration in the LC as a measure of the susceptibility to hypoxia. (Davies et al., 2013; Mintun et al., 2001) The 10th percentile was used as the definition of the minimum value to reduce the influence of possible numerical artifacts or of regions too small to have a physiological impact. (Hua et al., 2020; Voorhees et al., 2020) We evaluated other percentile levels and obtained equivalent results.

2.6 Statistical analysis

ANOVA was used to determine the influence and statistical significance of the factor and interaction effects. (Dar et al., 2002; Montgomery, 2017) The percentage of the total sum of squares corrected by the mean was used to represent the approximate contribution of each factor and interaction to the variance of the response, providing a measure of influence. (Sigal, 2009; Sigal et al., 2005a) A factor or interaction had to contribute at least 5% to the total variance of the response to be deemed influential in a physiologically significant way. For statistical significance, we used $P < 0.01$, and the contribution had to be greater than the residual. In this work, interactions refer to two-factor interactions. Higher-order interactions were found to have much weaker effects and are therefore not presented or discussed.

The response variable was transformed to improve the normality of the response and the residual, satisfy the requirements of ANOVA, and allow factor effects to be added in an unbiased

fashion. A traditional Box-Cox analysis and plot method was used to determine the optimal transformation for the response. (Box et al., 2005) We found that the optimal transformation was a power transformation. For plotting, the response was converted back to the original scale. The experiment was designed and analyzed with commercial software (Design-Expert, version 7; Stat-Ease, Inc., Minneapolis, MN).

3. Results

The 3D LC vascular network and the blood flow within were quite complex (**Figure 3** and **Video 1**). The flow rate was relatively high at the periphery, where blood flows in from the circle of Zinn-Haller, and at the center, where blood drains through the central retinal vein. The oxygen distribution in the LC was heterogeneous. Regions with low oxygen did not colocalize precisely with those of low blood flow. This is important as it indicates that it is not sufficient to compute or measure the blood flow to understand the oxygenation.

Figure 4 shows the distributions of blood pressure and flow velocity through the baseline model. The flow was primarily from the peripheral to the center, consistent with current understanding of ONH hemodynamics. (Hayreh 2001) The flow pattern can also be discerned in **Figure 5** and **Video 2**.

Scatterplots of minimum oxygen concentration as a function of each of the factors are shown in **Figure 6**. The plots are sorted according to the strength of the factor effects. A clear positive association is discernible for the vessel diameter. Weak negative and positive associations are still discernible for the oxygen consumption rate and arteriole pressure, respectively. ANOVA revealed that the factors affecting the minimum oxygen concentration the most were the vessel diameter, neural tissue oxygen consumption rate, and arteriole pressure (P's < 0.001) (**Figure 7**). These three factors and their interactions accounted for the majority of variance (87%) in the minimum oxygen concentration.

Our primary goal was to understand the factors affecting LC oxygen. As noted in the methods, to estimate the oxygen, it was necessary to predict the LC blood flow. This is also an outcome of potential interest, and thus we examined the association between LC blood flow and all the factors, and computed the ranking of factors and interactions. These results, while interesting, are not central to our goals, and thus we show them as **Supplementary Figures S1 and S2**. Our results show that the most influential factors on the LC oxygen were not just those influencing the blood flow. For example, the oxygen consumption rate had the second strongest influence on the LC oxygen, but had little effect on the LC blood flow. Again, this shows that, to predict LC oxygenation, it is not sufficient to measure the blood flow. The boundary pressures also had different effects on the LC oxygen and blood flow. As an example, the pre-laminar pressure impacted the LC blood flow more than the oxygen.

There were strong interactions between the three influential factors on the minimum oxygen concentration in the LC (**Figure 7**). An improved understanding of the role of factor interactions can be gained by examining the interaction plot in **Figure 8**. An interaction plot shows the effects

of two factors on a response, with all other factors constant (in this case at the baseline). The interaction plot illustrates that: 1) the impact of vessel diameter was more substantial when the arteriole pressure was lower, and 2) the impact of arteriole pressure was more substantial when the vessel diameter was smaller.

Figure 9 illustrates the effects on blood flow and oxygen concentration of the two most influential factors, vessel diameter and oxygen consumption rate.

4. Discussion

Our goal was to identify the factors with the strongest influence on the LC oxygenation. Specifically, we focused on the minimum (10th percentile) oxygen concentration – as a measure of the risk of hypoxia. Our models predicted that the vessel diameter, tissue oxygen consumption rate, and arteriole pressure had the strongest influence on the minimum oxygen concentration in the LC. There were strong interactions between the influential factors. Our models also predicted that LC oxygenation and blood flow did not overlap perfectly. Before we go any further, we remind readers that the model predictions reported herein were obtained from a single eye, and thus that it is impossible to know how general they are. More eyes must be studied before general conclusions can be drawn. Our intent in this work was to illustrate a workflow from vascular network reconstruction to parametric analysis on LC oxygenation. This is important information that could help understand ONH physiology and pathology previously unavailable for a specific eye. Below we discuss in detail the main findings and potential implications, followed by a detailed discussion of the limitations of the methods.

Vessel diameter was the strongest influential factor on the LC oxygenation

Our models predicted that the minimum oxygen concentration in the LC was positively associated with the vessel diameter. This can be understood as follows: an increase in vessel diameter decreases the flow resistance, increasing the blood flow rate, resulting in more efficient oxygen transport and a higher oxygen concentration in the LC. Tissues in the LC experience stretch, compression, and shearing under IOP. (Hua et al., 2020; Ma et al., 2020; Sigal et al., 2014; Voorhees et al., 2020; Voorhees et al., 2017b) Such deformations can be transferred to the vessels in the LC, resulting in changes in vessel tortuosities and diameters. (Brazile et al., 2020; Causin et al., 2014; Chuangsuwanich et al., 2020) For example, reduced vessel diameters due to elevated IOP have been observed experimentally in the rat ONH, (Moreno et al., 2014) and suggested by computational models. (Causin et al., 2014) Vessels may be constricted due to pericyte action, although whether there are pericytes in the LC remains unclear. (Alarcon-Martinez et al., 2020; Tovar-Vidales et al., 2016) The predictions from our models were made under the

assumption that all vessels had the same diameter. We will address the rationale for this choice later in the Limitations.

Oxygen consumption rate had the second strongest influence on the LC oxygenation

The minimum oxygen concentration in the LC was negatively associated with the oxygen consumption rate of neural tissues. This seems reasonable, as neural tissues with a higher consumption rate would consume more oxygen within a fixed time interval, resulting in less oxygen remaining in the LC. It is important to consider that we assumed neural tissue consumption rate to be uniform throughout the LC. It is possible that LC regions vary in consumption rate due to variations in the amount, type or activity of neural tissues (including axons, astrocytes, and other cells). For example, the consumption rate in larger pores could be higher since there are proportionally more high-oxygen-consumption neural tissues than low-oxygen-consumption collagen, resulting in the tissues within these pores more susceptible to hypoxia-induced damage. Due to the pressure gradient across the LC resulting from differences between IOP and CSFP, maintaining axonal transport may also result in consumption rates varying over the LC or over time. (Feola et al., 2017; Tran et al., 2017a; Wang et al., 2017; Zhu et al., 2021) With current techniques, it is challenging to measure in vivo the oxygen consumption rate in the LC.

Arteriole pressure ranked the third strongest influential factor on the LC oxygenation

The minimum oxygen concentration in the LC was positively associated with the arteriole pressure. A higher arteriole pressure would facilitate blood flow toward the LC and supply more oxygen to neural tissues. Since arteriole pressure is related to systemic blood pressure, it is plausible that individuals with a higher blood pressure may have a lower risk for developing ischemia-induced optic neuropathy, such as glaucoma. However, evidence for the role of blood pressure on glaucoma remains controversial. (He et al., 2011) Some studies have linked glaucoma with low blood pressure, (Graham et al., 1995; Hayreh et al., 1994) whereas others have reported a significant positive association between high blood pressure and glaucoma. (Bonomi et al., 2000; Dielemans et al., 1995; Hulsman et al., 2007) Study results are much more consistent when instead of blood pressure they have considered ocular perfusion pressure, which is defined as the difference between blood pressure and IOP. Low ocular perfusion pressure has consistently been linked to glaucoma in population studies. (Bonomi et al., 2000; Quigley et al., 2001; Tielsch et al., 1995)

The anterior and posterior boundary blood pressures are related to IOP and CSFP, respectively. Given the roles of IOP and CSFP on glaucomatous neuropathy, (Tran et al., 2017a;

Wang et al., 2017) it was somewhat unexpected that the anterior and posterior boundary blood pressures did not play a larger role in blood flow and oxygenation. The possible reasons are given below: First, we did not incorporate potential effects of pressure-induced vessel deformation. This is likely to underestimate the effects of the anterior and posterior boundary blood pressures. Second, we analyzed the vascular network of a healthy monkey eye. Thus, for conditions that are modeled around the normal, it seems reasonable to expect that this eye would not suffer much adverse effects. Having identified the factors with the strongest influences on ONH hemodynamics will shed light on the characteristics that can potentially make an eye more sensitive to the pressures and susceptible to pathology. Studies using OCT-A suggest that vessel density in the pre-laminar region may be lower in glaucoma eyes than in healthy ones, (Numa et al., 2018; Rao et al., 2017) although like all cross-sectional studies it remains unclear if these differences are indicative of susceptibility to glaucoma or a consequence. Third, the model predictions reported in this study were obtained from a single eye. More eyes must be studied before we can really consider the roles of the anterior and posterior boundary blood pressures.

LC oxygenation and blood flow did not overlap perfectly

The strong interest in characterizing and understanding the causes of neural tissue damage in glaucoma have prompted the development and application of many tools to study the ONH in vivo. Measures of blood flow can be obtained, for instance, using optical coherence tomography angiography, (De Carlo et al., 2015; Jia et al., 2012) Doppler ultrasound, (Butt et al., 1995; Vosborg et al., 2020) and laser speckle flowgraphy (Shiga et al., 2016; Sugiyama et al., 2010; Wang et al., 2012). Blood flow is of great relevance and thus these tools have provided important insight into the physiology and pathology of the posterior pole. Blood flow, however, is not a perfect surrogate measure of oxygenation. Our results show both that LC blood flow and oxygenation do not overlap perfectly, and that tissue oxygen consumption is a major factor in minimum oxygenation. Thus, to understand the risk of hypoxia, it is essential to develop experimental techniques that measure directly tissue oxygenation and consumption. To the best of our knowledge, despite important advances in recent years, (Pi et al., 2020; Soetikno et al., 2018), experimental measurement of oxygenation is still not suitable for the in vivo study of the LC. We posit that computational models, like the ones in this work, limited as they are by the simplifications and necessary assumptions, represent an invaluable opportunity to improve our understanding of ONH oxygenation and risk of hypoxia.

In our models, low oxygen concentration tended to be located in the central region of the canal, whereas neural tissue in the canal periphery is often thought to be damaged earlier in glaucoma.

However, tissues likely also vary in their metabolic needs and sensitivity to low oxygen, and thus there may not be a simple relationship between low oxygen concentration and early damage.

To the best of our knowledge, this is the first study modeling 3D eye-specific blood flow and oxygen concentration in the LC. Previous studies modeling LC hemodynamics and oxygenation were based on highly simplified 2D generic LC vascular networks, resulting in their predictions to be less representative of the physiologic conditions. (Carichino et al., 2012; Causin et al., 2014; Chuangsuwanich et al., 2016; Chuangsuwanich et al., 2020) Constructing a 3D eye-specific LC vascular network with pre and retro-laminar vessels allowed us to apply more realistic pressure boundary conditions than is possible in highly simplified generic networks. We considered arteriole and venule pressures for inflow and outflow in very much the same way as previous studies, but we were also able to consider the effects of IOP and CSFP that are potentially crucial to understand susceptibility to glaucoma. (Brazile et al., 2020; Hua et al., 2018; Morgan et al., 1998) Although the direct influences of these two pressures on the LC blood flow and oxygen concentration were weaker than those of arteriole and venule pressures, their mechanical effects on LC hemodynamics and oxygenation could be substantial in other ways. For example, changes of either pressure could lead to tissue distortion that would affect vessel diameter, and in turn blood perfusion and oxygen delivery. (Carichino et al., 2012; Causin et al., 2014; Chuangsuwanich et al., 2020) Changes in IOP and CSFP could also alter the patterns of blood flow and oxygenation through the LC. In this work we focused only on the minimum oxygenation, and did not explore yet the patterns or distribution of the oxygenation. The ability to separate the direct and indirect effects of factors is one of the most useful strengths of computational modeling compared with experiments. (Voorhees et al., 2018) Future studies should look further into the effects of these two pressures on blood flow and oxygenation given their known influence in ONH biomechanics.

We want to highlight another strength of this study. Our experimental design and analysis allowed us to evaluate the interactions between factors, namely how the effects of factors depend on each other. In biological systems, factors are often related, vary together, or have effects that depend on each other. The importance of factor interactions has been demonstrated in various areas of biomechanics, including the eye. (Dar et al., 2002; Liu and Roberts, 2005; Sigal et al., 2011a; Sigal et al., 2011b) Ignoring factor interactions causes not only to miss that potentially crucial insight, but it can lead to severely over or underestimating the strength of individual factors. (Anderson and Whitcomb, 2017) It is unclear why other studies have not accounted for factor interactions. One potential explanation could be that the LC is already quite complex, and thus the authors opted for a simple method for the study. This work demonstrates that, despite the

complexity of the LC vasculature and the blood flow within, it is possible to study and quantify factor interactions in a systematic way. Computational models provide an ideal platform for exploring LC hemodynamics and oxygenation and identifying the key factors and their interactions to inform experimental design and analysis.

Limitations

It is important to acknowledge the limitations of this study. A salient one, noted above, is that the model predictions reported herein were based on a single eye. Our work, therefore, serves as a demonstration of what can be done and provides insight into one eye, or a virtual “family of eyes” with the same vessel network and which differ only in the parameters varied. Given the high inter-eye variability in other aspects of ONH morphology, readers should be cautious and not assume that our findings are general.

We reconstructed the 3D LC vascular network from a healthy monkey eye. Although similar to human eyes regarding their size and collagenous LC and several aspects of pathophysiology, monkey eyes have distinct structural characteristics from human eyes. (Burgoyne et al., 2005) For example, monkey LCs have a trough-like shape, without the characteristic central ridge that makes human LCs saddle-rut shaped. (Tran et al., 2017c) Differences may also exist in the LC vasculature. The extent to which the monkey and human LC vasculatures are truly comparable remains to be established. Future work should include the vasculatures from human eyes, eyes of different ages, and diseased eyes to further understand LC hemodynamics and oxygenation.

The integrity of the reconstructed vascular network largely depends on the quality of vessel perfusion. Perfusion of vasculature ex vivo may not reach all vascular tracts. This can be due in part to clotting and/or insufficient perfusate volume, or tissue swelling. To prevent vascular obstruction, we made efforts to minimize the time between the death of the animal and perfusion. For instance, we were able to obtain the monkey head within minutes of sacrifice and begin the perfusion process via the carotid arteries within an hour of sacrifice. We also performed extensive flushing of vasculature with PBS to remove blood from vessels. A large volume (50 mL) of dye was perfused for the eye to ensure sufficient labeling. Before cryosectioning, the eye was examined under a fluorescence microscope for labeling of retinal and choroidal vessels. The eye demonstrated continuous staining of vessels and did not show any notable leaks. Whereas the presence of unlabeled vessels is possible, we believe we labeled the majority of vessels present. Additionally, lack of labeling in some vessels does not affect the main conclusions of this study.

We imaged coronal cryosections through the LC to visualize the blood vessels. There may have been artifacts induced by formalin fixation and sectioning, such as tissue distortion or

shrinkage. However, we have shown previously that our method has minimal effects on changing the shape or size of ocular tissues. (Jan et al., 2015; Tran et al., 2017b) Future work could use fiducial markers to correct for any tissue warping during sectioning. (Sigal et al., 2005b) In addition, the cryosections for vasculature reconstruction were 16-µm-thick, resulting in a more limited depth resolution than the in-plane resolution. A higher depth resolution is desired for higher fidelity 3D reconstruction of the LC vasculature in future studies. Techniques like a tape transfer system can significantly reduce the minimum section thickness to as low as 2 µm and could be a potential candidate. (Golubeva et al., 2013)

Like other studies of LC hemodynamics before, (Causin et al., 2016; Chuangsuwanich et al., 2016; Chuangsuwanich et al., 2020) we assumed that all vessels in the LC had the same diameter. This was necessary because there are no studies providing detailed maps of vessel diameter. Our technique for reconstructing the vessel network could be leveraged to obtain this information. However, this is substantially more complicated in practice than it may seem on first inspection. For instance, post-mortem diameter and cross-sectional shape may differ from that in vivo due to the absence of blood pressure and/or tissue swelling. In addition, some of the vessels are within the connective tissue beams, and others are outside. (Brazile et al., 2020) This may affect how the vessels respond to changes in the pressures within (local blood pressure) or outside (IOP and CSFP). Vessel diameters in vivo could be affected by tissue distortions, as noted before. They could also be affected by autoregulation, which we have not yet considered in our models. Impaired autoregulation in the ONH has been postulated to play a role in individual susceptibility to glaucomatous optic neuropathy. (Prada et al., 2016) However, experimental measurements of autoregulation have been hampered by many of the same challenges that affect measurements of blood flow deep within the ONH, and thus the best information is from the pre-laminar region. For the pre-laminar region, the studies have shown that the blood flow is both highly sensitive to IOP levels, and that there is a highly refined autoregulatory system. (Sugiyama et al., 2010; Wang et al., 2001) The autoregulatory systems in the deep ONH and LC, however, are thought to be different and independent, and remain uncharacterized in vivo. (Burgoyne et al., 2005; Hayreh, 1996; Hayreh et al., 1994; Wang et al., 2001) Further work, potentially involving variations of the reconstruction technique used for this work coupled with in vivo imaging, could help provide detailed information on vessel diameters and the potential role of autoregulation in the LC. The parametric analysis in this work seems like a reasonable first step given the variability and uncertainty in the vessel diameters and the difficulty in obtaining reliable experimental data of the physiologic values.

We assumed the blood flow within a given vessel was one-dimensional, such that only the average flow velocity was solved for each cross-section of a vessel. We, and others, (Causin et al., 2016; Chuangsuwanich et al., 2016; Chuangsuwanich et al., 2020; Lu et al., 2021; Secomb et al., 2004) have followed this approach, as it is computationally efficient, and most importantly, it is a reasonable approximation of blood flow in microvessels. We also assumed the flow to be steady (unvarying in time) and laminar (free of turbulence). The Reynolds number, *i.e.*, the ratio of inertial forces to viscous forces, of blood flowing in microvessels is generally in the range of 10^{-3} to about 1, (Pries and Secomb, 2008) indicating the flow is laminar. Therefore, it was reasonable to disregard the effects of fluid inertia in microvessels.

It is very important to consider that we did not incorporate the pressure-induced vessel deformations in this study. Our intent was to provide a first approximation to the regional hemodynamics, that later must be refined to incorporate other effects. We are not the first to follow this approach. Other studies of ONH hemodynamics have also explored blood flow independently from pressure-induced vessel deformations. (Chuangsuwanich et al., 2016) The extent to which the pressure-induced vessel deformations may affect the flow and oxygen distribution remains unknown. Experiments and numerical models of pressure-induced ONH deformations suggest that the distortions are typically in the range of single digits for compression. (Ma et al., 2020; Midgett et al., 2020; Sigal et al., 2014; Voorhees et al., 2017b; Zhang et al., 2015) Although these may seem small, ONH flow is complex and it is important to not assume that the effects on oxygenation will also be small.

Since we did not consider the pressure-induced vessel deformations, we are yet to determine whether the action of the pre- and retro-laminar tissue pressures could result in collapse of vessels inside or outside collagen beams. It is potentially important to consider the interactions between blood vessels and collagen beams, and the effects of collagen beams on the pressure-induced vessel deformations, which will be studied in the future.

Another elegant and powerful approach to model the LC was followed by (Causin et al., 2014). Their method allowed them to account simultaneously for solid deformations and fluid flow through the solid structure. The approach, however, does not consider specific blood vessels and is therefore not directly suitable for the type of model in this study.

We assumed the oxygen consumption rate of neural tissues to be uniform throughout the LC. As noted above, the oxygen consumption rate may vary with regions and/or pressure gradients in the LC. It may be advantageous to incorporate region- and pressure-dependent neural tissue oxygen consumption rate in future studies.

Our models have not been validated yet. This is extremely difficult because accurate in vivo measures of LC blood flow and oxygen concentration are not possible with current imaging techniques. As noted above, there have been recent promising efforts to characterize retinal capillary oxygen concentration using visible-light optical coherence tomography, (Pi et al., 2020) but this remains out of reach. We note that our model-predicted blood flow and oxygen concentration lie within normal biological ranges in other tissues with comparable capillary diameters. (Akons et al., 2017; Mintun et al., 2001) Nevertheless, until the models have been properly validated, in this study we have focused on a statistical approach comparing between models. This provides information fundamental to understand the role of the various interacting factors.

In summary, we have developed 3D eye-specific models of the LC vascular network. Our models predicted that the vessel diameter, neural tissue oxygen consumption rate, and arteriole pressure had the strongest influence on the LC oxygenation. Considering the vessel diameter was the most influential factor, situations that reduce the diameter, such as IOP or gaze-induced tissue deformation, may particularly contribute to decreased LC oxygen concentration.

Acknowledgements

Supported by National Institutes of Health R01-EY023966, R01-EY028662, R01-EY031708, P30-EY008098, R01-HD045590, R01-HD083383, and T32-EY017271; Eye and Ear Foundation (Pittsburgh, Pennsylvania), Research to Prevent Blindness and the Brightfocus Foundation.

Conflict of Interest: Y. Hua, None; Y. Lu, None; J. Walker, None; P.Y. Lee, None; Q. Tian, None; H. McDonald, None; P. Pallares, None; F. Ji, None; B.L. Brazile was at the University of Pittsburgh when he contributed to this work. He is now at Baxter; B. Yang, None; A.P. Voorhees was at the University of Pittsburgh when he contributed to this work. He is now at Johnson & Johnson; I.A. Sigal, None.

References

Akons, K., Dann, E.J., Yelin, D., 2017. Measuring blood oxygen saturation along a capillary vessel in human. Biomedical Optics Express 8, 5342-5348.

Alarcon-Martinez, L., Villafranca-Baughman, D., Quintero, H., Kacerovsky, J.B., Dotigny, F., Murai, K.K., Prat, A., Drapeau, P., Di Polo, A., 2020. Interpericyte tunnelling nanotubes regulate neurovascular coupling. Nature 585, 91-95.

An, D., Pulford, R., Morgan, W.H., Yu, D.-Y., Balaratnasingam, C., 2021. Associations between capillary diameter, capillary density, and microaneurysms in diabetic retinopathy: A high-resolution confocal microscopy study. Translational Vision Science & Technology 10, 6-6.

Anderson, M.J., Whitcomb, P.J., 2017. DOE simplified: practical tools for effective experimentation. CRC press.

Bonomi, L., Marchini, G., Marraffa, M., Bernardi, P., Morbio, R., Varotto, A., 2000. Vascular risk factors for primary open angle glaucoma: the Egna-Neumarkt Study. Ophthalmology 107, 1287-1293.

Box, G.E., Hunter, J.S., Hunter, W.G., 2005. Statistics for experimenters: design, discovery and innovation. Wiley-Interscience 639.

Brazile, B.L., Hua, Y., Jan, N.-J., Wallace, J., Gogola, A., Sigal, I.A., 2018. Thin Lamina Cribrosa Beams Have Different Collagen Microstructure Than Thick Beams. Investigative ophthalmology & visual science 59, 4653-4661.

Brazile, B.L., Yang, B., Waxman, S., Lam, P., Voorhees, A.P., Hua, Y., Loewen, R.T., Loewen, N.A., Rizzo III, J.F., Jakobs, T.C., Sigal, I.A., 2020. Lamina cribrosa capillaries straighten as intraocular pressure increases. Investigative Ophthalmology & Visual Science 61, 2-2.

Burgoyne, C.F., Downs, J.C., Bellezza, A.J., Suh, J.K., Hart, R.T., 2005. The optic nerve head as a biomechanical structure: a new paradigm for understanding the role of IOP-related stress and strain in the pathophysiology of glaucomatous optic nerve head damage. Progress in Retinal and Eye Research 24, 39-73.

Butt, Z., McKillop, G., O'Brien, C., Allan, P., Aspinall, P., 1995. Measurement of ocular blood flow velocity using colour Doppler imaging in low tension glaucoma. Eye 9, 29-33.

Carichino, L., Guidoboni, G., Arieli, Y., Siesky, B.A., Harris, A., 2012. Effect of lamina cribrosa deformation on the hemodynamics of the central retinal artery: a mathematical model. Investigative Ophthalmology & Visual Science 53, 2836-2836.

Causin, P., Guidoboni, G., Harris, A., Prada, D., Sacco, R., Terragni, S., 2014. A poroelastic model for the perfusion of the lamina cribrosa in the optic nerve head. Mathematical Biosciences 257, 33-41.

Causin, P., Guidoboni, G., Malgaroli, F., Sacco, R., Harris, A., 2016. Blood flow mechanics and oxygen transport and delivery in the retinal microcirculation: multiscale mathematical modeling and numerical simulation. Biomechanics Modeling in Mechanobiology 15, 525-542.

Chu, Y.-C., Chen, C.-Z., Lee, C.-H., Chen, C.-W., Chang, H.-Y., Hsiue, T.-R., 2003. Prediction of arterial blood gas values from venous blood gas values in patients with acute respiratory failure receiving mechanical ventilation. Journal of the Formosan Medical Association 102, 539-543.

Chuangsuwanich, T., Birgersson, K.E., Thiery, A., Thakku, S.G., Leo, H.L., Girard, M.J., 2016. Factors influencing lamina cribrosa microcapillary hemodynamics and oxygen concentrations. Investigative Ophthalmology & Visual Science 57, 6167-6179.

Chuangsuwanich, T., Hung, P.T., Wang, X., Liang, L.H., Schmetterer, L., Boote, C., Girard, M.J.A., 2020. Morphometric, hemodynamic, and biomechanical factors influencing blood flow and oxygen concentration in the human lamina cribrosa. Investigative Ophthalmology & Visual Science 61, 3-3.

Dar, F.H., Meakin, J.R., Aspden, R.M., 2002. Statistical methods in finite element analysis. Journal of Biomechanics 35, 1155-1161.

Davies, A.L., Desai, R.A., Bloomfield, P.S., McIntosh, P.R., Chapple, K.J., Linington, C., Fairless, R., Diem, R., Kasti, M., Murphy, M.P., 2013. Neurological deficits caused by tissue hypoxia in neuroinflammatory disease. Annals of Neurology 74, 815-825.

De Carlo, T.E., Romano, A., Waheed, N.K., Duker, J.S., 2015. A review of optical coherence tomography angiography (OCTA). International Journal of Retina and Vitreous 1, 5.

Dielemans, I., Vingerling, J.R., Algra, D., Hofman, A., Grobbee, D.E., de Jong, P.T., 1995. Primary open-angle glaucoma, intraocular pressure, and systemic blood pressure in the general elderly population: the Rotterdam Study. Ophthalmology 102, 54-60.

Fechtner, R.D., Weinreb, R.N., 1994. Mechanisms of optic nerve damage in primary open angle glaucoma. Survey of Ophthalmology 39, 23-42.

Feola, A.J., Coudrillier, B., Mulvihill, J., Geraldes, D.M., Vo, N.T., Albon, J., Abel, R.L., Samuels, B.C., Ethier, C.R., 2017. Deformation of the lamina cribrosa and optic nerve due to changes in cerebrospinal fluid pressure. Investigative ophthalmology & visual science 58, 2070-2078.

Feola, A.J., Myers, J.G., Raykin, J., Mulugeta, L., Nelson, E.S., Samuels, B.C., Ethier, C.R., 2016. Finite element modeling of factors influencing optic nerve head deformation due to intracranial pressure. Investigative ophthalmology & visual science 57, 1901-1911.

Golubeva, Y.G., Smith, R.M., Sternberg, L.R., 2013. Optimizing frozen sample preparation for laser microdissection: assessment of CryoJane tape-transfer system®. PlOS ONE 8, e66854.

Graham, S.L., Drance, S.M., Wijsman, K., Douglas, G.R., Mikelberg, F.S., 1995. Ambulatory blood pressure monitoring in glaucoma: the nocturnal dip. Ophthalmology 102, 61-69.

Groebe, K., 1990. A versatile model of steady state O2 supply to tissue. Application to skeletal muscle. Biophysical Journal 57, 485-498.

Hayreh, S., 1996. The optic nerve head circulation in health and disease. Ophthalmic Literature 2, 111.

Hayreh, S.S., 1969. Blood supply of the optic nerve head and its role in optic atrophy, glaucoma, and oedema of the optic disc. The British journal of ophthalmology 53, 721-748.

Hayreh, S.S., Zimmerman, M.B., Podhajsky, P., Alward, W.L., 1994. Nocturnal arterial hypotension and its role in optic nerve head and ocular ischemic disorders. American Journal of Ophthalmology 117, 603-624.

He, Z., Vingrys, A.J., Armitage, J.A., Bui, B.V., 2011. The role of blood pressure in glaucoma. Clinical and Experimental Optometry 94, 133-149.

Hill, A.V., 1921. The combinations of haemoglobin with oxygen and carbon monoxide, and the effects of acid and carbon dioxide. Biochemical Journal 15, 577-586.

Hsu, R., Secomb, T.W., 1989. A Green's function method for analysis of oxygen delivery to tissue by microvascular networks. Mathematical Biosciences 96, 61-78.

Hua, Y., Tong, J., Ghate, D., Kedar, S., Gu, L., 2017. Intracranial pressure influences the behavior of the optic nerve head. Journal of Biomechanical Engineering 139, 031003.

Hua, Y., Voorhees, A.P., Jan, N.-J., Wang, B., Waxman, S., Schuman, J.S., Sigal, I.A., 2020. Role of radially aligned scleral collagen fibers in optic nerve head biomechanics. Experimental Eye Research 199, 108188.

Hua, Y., Voorhees, A.P., Sigal, I.A., 2018. Cerebrospinal fluid pressure: Revisiting factors influencing optic nerve head biomechanics. Investigative Ophthalmology & Visual Science 59, 154-165.

Hulsman, C.A., Vingerling, J.R., Hofman, A., Witteman, J.C., de Jong, P.T., 2007. Blood pressure, arterial stiffness, and open-angle glaucoma: the Rotterdam study. Archives of Ophthalmology 125, 805-812.

Jan, N.-J., Gomez, C., Moed, S., Voorhees, A.P., Schuman, J.S., Bilonick, R.A., Sigal, I.A., 2017a. Microstructural crimp of the lamina cribrosa and peripapillary sclera collagen fibers. Investigative Ophthalmology & Visual Science 58, 3378-3388.

Jan, N.J., Grimm, J.L., Tran, H., Lathrop, K.L., Wollstein, G., Bilonick, R.A., Ishikawa, H., Kagemann, L., Schuman, J.S., Sigal, I.A., 2015. Polarization microscopy for characterizing fiber orientation of ocular tissues. Biomed Opt Express 6, 4705-4718.

Jan, N.J., Lathrop, K., Sigal, I.A., 2017b. Collagen Architecture of the Posterior Pole: High-Resolution Wide Field of View Visualization and Analysis Using Polarized Light Microscopy. Invest Ophthalmol Vis Sci 58, 735-744.

Jerman, T., Pernuš, F., Likar, B., Špiclin, Ž., 2016. Enhancement of vascular structures in 3D and 2D angiographic images. IEEE Transactions on Medical Imaging 35, 2107-2118.

Jia, Y., Morrison, J.C., Tokayer, J., Tan, O., Lombardi, L., Baumann, B., Lu, C.D., Choi, W., Fujimoto, J.G., Huang, D., 2012. Quantitative OCT angiography of optic nerve head blood flow. Biomedical Optics Express 3, 3127-3137.

Lee, P.-Y., Walker, J., Hua, Y., Brazile, B., Sigal, I.A., 2021. Integrating capillary flow modeling and geometric quantification into reconstructed 3D capillary networks of the optic nerve head, Summer Biomechanics, Bioengineering, and Biotransport Conference, Virtual meeting.

Levitzky, M., Henkind, P., 1969. Angioarchitecture of the optic nerve: II. Lamina cribrosa. American Journal of Ophthalmology 68, 986-996.

Li, Y., Song, Y., Zhao, L., Gaidosh, G., Laties, A.M., Wen, R., 2008. Direct labeling and visualization of blood vessels with lipophilic carbocyanine dye DiI. Nature protocols 3, 1703-1708.

Liu, J., Roberts, C.J., 2005. Influence of corneal biomechanical properties on intraocular pressure measurement: quantitative analysis. Journal of Cataract & Refractive Surgery 31, 146-155.

Lu, Y., Hu, D., Ying, W., 2021. A fast numerical method for oxygen supply in tissue with complex blood vessel network. PloS One 16, e0247641.

Ma, Y., Pavlatos, E., Clayson, K., Kwok, S., Pan, X., Liu, J., 2020. Three-dimensional inflation response of porcine optic nerve head using high-frequency ultrasound elastography. Journal of Biomechanical Engineering 142, 051013.

Midgett, D.E., Jefferys, J.L., Quigley, H.A., Nguyen, T.D., 2020. The inflation response of the human lamina cribrosa and sclera: Analysis of deformation and interaction. Acta Biomaterialia 106, 225-241.

Mintun, M.A., Lundstrom, B.N., Snyder, A.Z., Vlassenko, A.G., Shulman, G.L., Raichle, M.E., 2001. Blood flow and oxygen delivery to human brain during functional activity: theoretical modeling and experimental data. Proceedings of the National Academy of Sciences 98, 6859-6864.

Montgomery, D.C., 2017. Design and analysis of experiments. John wiley & sons.

Moreno, M., Ríos, M.C., Alba, C., Díaz, F., Villena, A., Figueroa-Ortiz, L.C., García-Campos, J., 2014. Morphological and morphometric changes in rat optic nerve microvessels in a glaucoma experimental model. Archivos de la Sociedad Espanola de Oftalmologia 89, 471-476.

Morgan, W.H., Yu, D.-Y., Alder, V.A., Cringle, S.J., Cooper, R.L., House, P.H., Constable, I.J., 1998. The correlation between cerebrospinal fluid pressure and retrolaminar tissue pressure. Investigative Ophthalmology & Visual Science 39, 1419-1428.

Mozaffarieh, M., Bärtschi, M., Henrich, P., Schoetzau, A., Flammer, J., 2014. Retinal venous pressure in the non-affected eye of patients with retinal vein occlusions. Graefes Arch Clin Exp Ophthalmol 252, 1569-1571.

Numa, S., Akagi, T., Uji, A., Suda, K., Nakanishi, H., Kameda, T., Ikeda, H.O., Tsujikawa, A., 2018. Visualization of the lamina cribrosa microvasculature in normal and glaucomatous

eyes: a wwept-source optical coherence tomography angiography study. Journal of Glaucoma 27, 1032-1035.

Pi, S., Hormel, T.T., Wei, X., Cepurna, W., Wang, B., Morrison, J.C., Jia, Y., 2020. Retinal capillary oximetry with visible light optical coherence tomography. Proceedings of the National Academy of Sciences 117, 11658-11666.

Prada, D., Harris, A., Guidoboni, G., Siesky, B., Huang, A.M., Arciero, J., 2016. Autoregulation and neurovascular coupling in the optic nerve head. Survey of Ophthalmology 61, 164-186.

Pries, A., Secomb, T., Gessner, T., Sperandio, M., Gross, J., Gaehtgens, P., 1994. Resistance to blood flow in microvessels in vivo. Circulation Research 75, 904-915.

Pries, A.R., Ley, K., Claassen, M., Gaehtgens, P., 1989. Red cell distribution at microvascular bifurcations. Microvascular research 38, 81-101.

Pries, A.R., Secomb, T.W., 2005. Microvascular blood viscosity in vivo and the endothelial surface layer. American Journal of Physiology-Heart and Circulatory Physiology 289, H2657-H2664.

Pries, A.R., Secomb, T.W., 2008. Blood flow in microvascular networks, Microcirculation. Elsevier, pp. 3-36.

Quigley, H., Anderson, D.R., 1976. The dynamics and location of axonal transport blockade by acute intraocular pressure elevation in primate optic nerve. Investigative Ophthalmology & Visual Science 15, 606-616.

Quigley, H.A., McKinnon, S.J., Zack, D.J., Pease, M.E., Kerrigan–Baumrind, L.A., Kerrigan, D.F., Mitchell, R.S., 2000. Retrograde axonal transport of BDNF in retinal ganglion cells is blocked by acute IOP elevation in rats. Investigative Ophthalmology & Visual Science 41, 3460-3466.

Quigley, H.A., Nickells, R.W., Kerrigan, L.A., Pease, M.E., Thibault, D.J., Zack, D.J., 1995. Retinal ganglion cell death in experimental glaucoma and after axotomy occurs by apoptosis. Investigative Ophthalmology & Visual Science 36, 774-786.

Quigley, H.A., West, S.K., Rodriguez, J., Munoz, B., Klein, R., Snyder, R., 2001. The prevalence of glaucoma in a population-based study of Hispanic subjects: Proyecto VER. Archives of Ophthalmology 119, 1819-1826.

Rao, H.L., Pradhan, Z.S., Weinreb, R.N., Riyazuddin, M., Dasari, S., Venugopal, J.P., Puttaiah, N.K., Rao, D.A., Devi, S., Mansouri, K., 2017. A comparison of the diagnostic ability of vessel density and structural measurements of optical coherence tomography in primary open angle glaucoma. PloS One 12, e0173930.

Roberts, M.D., Liang, Y., Sigal, I.A., Grimm, J., Reynaud, J., Bellezza, A., Burgoyne, C.F., Downs, J.C., 2010. Correlation between local stress and strain and lamina cribrosa connective tissue volume fraction in normal monkey eyes. Investigative ophthalmology & visual science 51, 295-307.

Secomb, T., Hsu, R., 1994. Simulation of O2 transport in skeletal muscle: diffusive exchange between arterioles and capillaries. American Journal of Physiology-Heart and Circulatory Physiology 267, H1214-H1221.

Secomb, T., Hsu, R., Beamer, N., Coull, B., 2000. Theoretical simulation of oxygen transport to brain by networks of microvessels: effects of oxygen supply and demand on tissue hypoxia. Microcirculation 7, 237-247.

Secomb, T., Hsu, R., Braun, R., Ross, J., Gross, J., Dewhirst, M., 1998. Theoretical simulation of oxygen transport to tumors by three-dimensional networks of microvessels, Oxygen Transport to Tissue XX. Springer, pp. 629-634.

Secomb, T.W., Hsu, R., Dewhirst, M., Klitzman, B., Gross, J., 1993. Analysis of oxygen transport to tumor tissue by microvascular networks. International Journal of Radiation Oncology, Biology, Physics 25, 481-489.

Secomb, T.W., Hsu, R., Park, E.Y., Dewhirst, M.W., 2004. Green's function methods for analysis of oxygen delivery to tissue by microvascular networks. Ann Biomed Eng 32, 1519-1529.

Shiga, Y., Kunikata, H., Aizawa, N., Kiyota, N., Maiya, Y., Yokoyama, Y., Omodaka, K., Takahashi, H., Yasui, T., Kato, K., 2016. Optic nerve head blood flow, as measured by laser speckle flowgraphy, is significantly reduced in preperimetric glaucoma. Current Eye Research 41, 1447-1453.

Sigal, I.A., 2009. Interactions between geometry and mechanical properties on the optic nerve head. Investigative ophthalmology & visual science 50, 2785-2795.

Sigal, I.A., Ethier, C.R., 2009. Biomechanics of the optic nerve head. Exp Eye Res 88, 799-807.

Sigal, I.A., Flanagan, J.G., Ethier, C.R., 2005a. Factors influencing optic nerve head biomechanics. Investigative Ophthalmology & Visual Science 46, 4189-4199.

Sigal, I.A., Flanagan, J.G., Tertinegg, I., Ethier, C.R., 2005b. Reconstruction of human optic nerve heads for finite element modeling. Technology and Health Care 13, 313-329.

Sigal, I.A., Flanagan, J.G., Tertinegg, I., Ethier, C.R., 2007. Predicted extension, compression and shearing of optic nerve head tissues. Experimental eye research 85, 312-322.

Sigal, I.A., Grimm, J.L., 2012. A few good responses: which mechanical effects of IOP on the ONH to study? Investigative ophthalmology & visual science 53, 4270-4278.

Sigal, I.A., Grimm, J.L., Jan, N.J., Reid, K., Minckler, D.S., Brown, D.J., 2014. Eye-specific IOP-induced displacements and deformations of human lamina cribrosa. Investigative Ophthalmology & Visual Science 55, 1-15.

Sigal, I.A., Yang, H., Roberts, M.D., Burgoyne, C.F., Downs, J.C., 2011a. IOP-induced lamina cribrosa displacement and scleral canal expansion: an analysis of factor interactions using parameterized eye-specific models. Investigative ophthalmology & visual science 52, 1896-1907.

Sigal, I.A., Yang, H., Roberts, M.D., Grimm, J.L., Burgoyne, C.F., Demirel, S., Downs, J.C., 2011b. IOP-induced lamina cribrosa deformation and scleral canal expansion: independent or related? Investigative ophthalmology & visual science 52, 9023-9032.

Soetikno, B.T., Beckmann, L., Zhang, X., Fawzi, A.A., Zhang, H.F., 2018. Visible-light optical coherence tomography oximetry based on circumpapillary scan and graph-search segmentation. Biomedical Optics Express 9, 3640-3652.

Stefánsson, E., Pedersen, D.B., Jensen, P.K., la Cour, M., Kiilgaard, J.F., Bang, K., Eysteinsson, T., 2005. Optic nerve oxygenation. Progress in Retinal and Eye Research 24, 307-332.

Sugiyama, T., Araie, M., Riva, C.E., Schmetterer, L., Orgul, S., 2010. Use of laser speckle flowgraphy in ocular blood flow research. Acta Ophthalmologica 88, 723-729.

Tielsch, J.M., Katz, J., Sommer, A., Quigley, H.A., Javitt, J.C., 1995. Hypertension, perfusion pressure, and primary open-angle glaucoma: a population-based assessment. Archives of Ophthalmology 113, 216-221.

Tovar-Vidales, T., Wordinger, R.J., Clark, A.F., 2016. Identification and localization of lamina cribrosa cells in the human optic nerve head. Experimental Eye Research 147, 94-97.

Tran, H., Grimm, J., Wang, B., Smith, M., Gogola, A., Nelson, S., Tyler-Kabara, E., Schuman, J., Wollstein, G., Sigal, I., 2017a. Mapping in-vivo optic nerve head strains caused by intraocular and intracranial pressures, Optical Elastography and Tissue Biomechanics IV. International Society for Optics and Photonics, p. 100670B.

Tran, H., Jan, N.-J., Hu, D., Voorhees, A., Schuman, J.S., Smith, M.A., Wollstein, G., Sigal, I.A., 2017b. Formalin fixation and cryosectioning cause only minimal changes in shape or size of ocular tissues. Scientific Reports 7, 1-11.

Tran, H., Wallace, J., Voorhees, A.P., Zhu, Z., Wang, B., Lucy, K.A., Schuman, J.S., Smith, M., Wollstein, G., Sigal, I.A., 2017c. Lamina cribrosa shape is different between humans and monkeys at baseline IOP and is changed differently with IOP elevations. Investigative Ophthalmology & Visual Science 58, 3157-3157.

Voorhees, A., Grimm, J., Bilonick, R., Kagemann, L., Ishikawa, H., Schuman, J., Wollstein, G., Sigal, I., 2016. What is a typical optic nerve head? Experimental eye research 149, 40-47.

Voorhees, A., Hua, Y., Sigal, I.A., 2018. Parametric analysis to identify biomechanical risk factors; Taking control of population diversity and experiment variability, in: Roberts, C.J., Dupps, W.J., Downs, J.C. (Eds.), Biomechanics of the Eye. Kugler publications.

Voorhees, A.P., Hua, Y., Brazile, B.L., Wang, B., Waxman, S., Schuman, J.S., Sigal, I.A., 2020. So-called lamina cribrosa defects may mitigate IOP-induced neural tissue insult. Investigative Ophthalmology & Visual Science 61, 15-15.

Voorhees, A.P., Jan, N.J., Austin, M.E., Flanagan, J.G., Sivak, J.M., Bilonick, R.A., Sigal, I.A., 2017a. Lamina cribrosa pore shape and size as predictors of neural tissue mechanical insult. Investigative Ophthalmology & Visual Science 58, 5336-5346.

Voorhees, A.P., Jan, N.J., Sigal, I.A., 2017b. Effects of collagen microstructure and material properties on the deformation of the neural tissues of the lamina cribrosa. Acta Biomaterialia 58, 278-290.

Vosborg, F., Malmqvist, L., Hamann, S., 2020. Non-invasive measurement techniques for quantitative assessment of optic nerve head blood flow. European Journal of Ophthalmology 30, 235-244.

Wang, B., Tran, H., Smith, M.A., Kostanyan, T., Schmitt, S.E., Bilonick, R.A., Jan, N.-J., Kagemann, L., Tyler-Kabara, E.C., Ishikawa, H., 2017. In-vivo effects of intraocular and intracranial pressures on the lamina cribrosa microstructure. PloS One 12, e0188302.

Wang, C., Bassingthwaighte, J., 2003. Blood flow in small curved tubes. Journal of Biomechanical Engineering 125, 910-913.

Wang, L., Cull, G., Cioffi, G.A., 2001. Depth of penetration of scanning laser Doppler flowmetry in the primate optic nerve. Archives of Ophthalmology 119, 1810-1814.

Wang, L., Cull, G.A., Piper, C., Burgoyne, C.F., Fortune, B., 2012. Anterior and posterior optic nerve head blood flow in nonhuman primate experimental glaucoma model measured by laser speckle imaging technique and microsphere method. Investigative Ophthalmology & Visual Science 53, 8303-8309.

Waxman, S., Brazile, B.L., Yang, B., Gogola, A.L., Lam, P., Voorhees, A.P., Rizzo, J.F., Jakobs, T.C., Sigal, I.A., 2021. Lamina cribrosa vessel and collagen beam networks are distinct. bioRxiv, 462932.

Zhang, L., Albon, J., Jones, H., Gouget, C.L., Ethier, C.R., Goh, J.C., Girard, M.J., 2015. Collagen microstructural factors influencing optic nerve head biomechanics. Investigative Ophthalmology & Visual Science 56, 2031-2042.

Zhu, Z., Waxman, S., Wang, B., Wallace, J., Schmitt, S.E., Tyler-Kabara, E., Ishikawa, H., Schuman, J.S., Smith, M.A., Wollstein, G., 2021. Interplay between intraocular and intracranial pressure effects on the optic nerve head in vivo. Experimental Eye Research, 108809.

Table 1. Constants used in the Green's function method.

Constants	Units	Values	References
Oxygen diffusion coefficient, D	$cm^3O_2\ cm^{-1}\ s^{-1}\ mmHg^{-1}$	6×10^{-10}	(Secomb et al., 2000)
Effective solubility of oxygen in blood, α_{eff}	$cm^3O_2/cm^3/mmHg$	3.1×10^{-5}	(Secomb et al., 2004)
Maximum oxygen consumption rate, M_0	$cm^3O_2\ (100\ cm^3)^{-1}\ min^{-1}$	5×10^{-4}	(Secomb et al., 2000)
Michaelis-Menten constant, P_0	mmHg	10.5	(Secomb et al., 2004)
Blood oxygen concentration at inflow boundary nodes, P_b	mmHg	75	(Chu et al., 2003)
Hemoglobin-bound oxygen content of red blood cells, C_0	cm^3O_2/cm^3	0.5	(Secomb et al., 2004)

Table 2. Factor baseline values and their ranges in the sensitivity analysis.

Factors	Units	Low	Baseline	High	References
Vessel diameter	µm	6.4	8	9.6	(Brazile et al., 2020)
O_2 consumption rate	cm^3O_2 $(100\ cm^3)^{-1}$ min^{-1}	4×10^{-4}	5×10^{-4}	6×10^{-4}	(Secomb et al., 2000)
Arteriole pressure	mmHg	40	50	60	(Chuangsuwanich et al., 2016)
Venule pressure	mmHg	12	15	18	(Mozaffarieh et al., 2014)
Pre-laminar pressure*	mmHg	16	20	24	(Hua et al., 2018)
Retro-laminar pressure*	mmHg	12.8	16	19.2	(Feola et al., 2016; Hua et al., 2018)
Inflow hematocrit	/	0.36	0.45	0.54	(Pries and Secomb, 2008)

* The baseline values of the pre- and retro-laminar pressures were determined with their low levels (-20%) equivalent to normal intraocular and cerebrospinal fluid pressures, respectively.

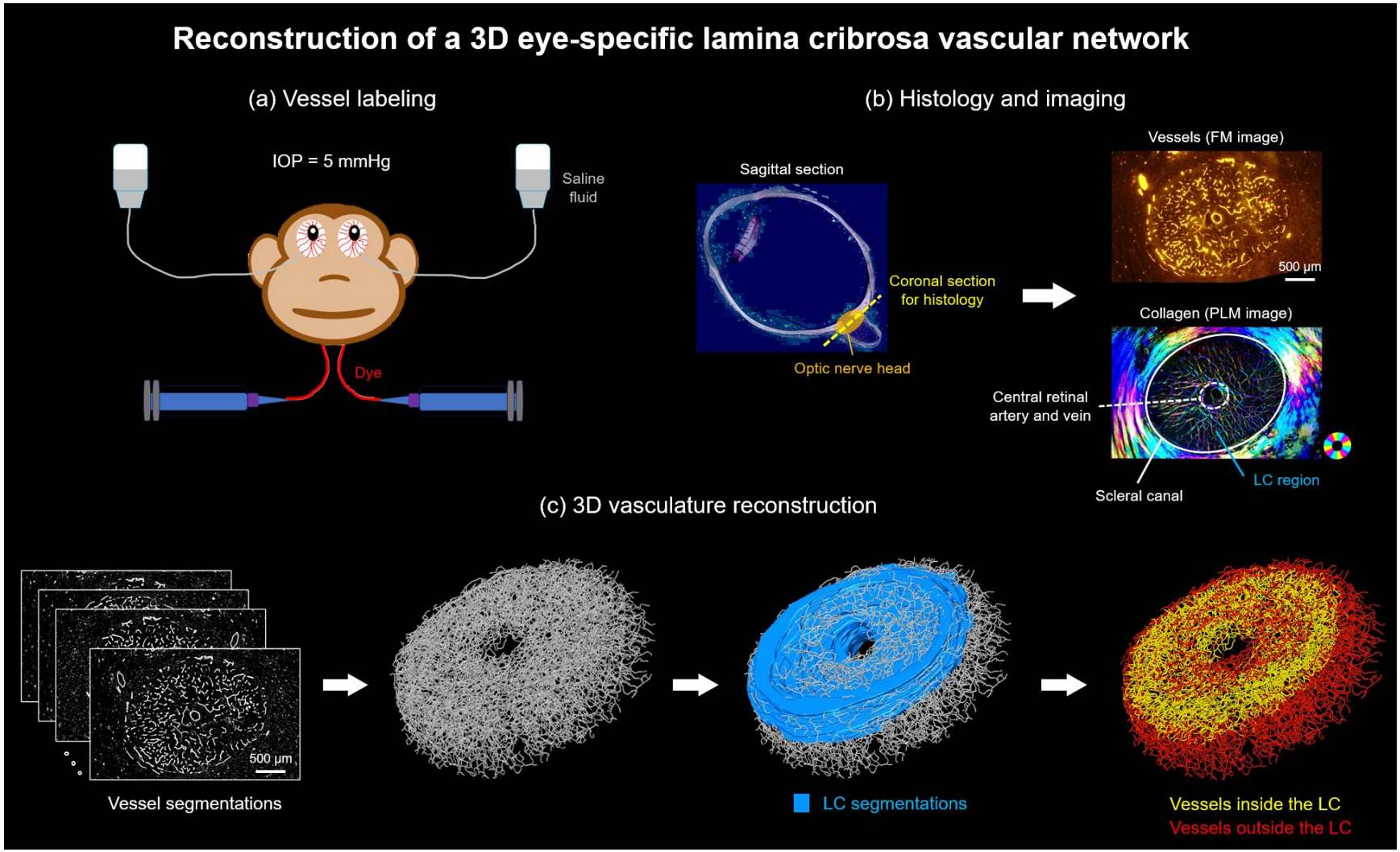

Figure 1. General approach for the reconstruction of a 3D eye-specific lamina cribrosa (LC) vascular network. **(a)** Vessels in the eye were labeled with a fluorescent dye, while IOP was set to 5 mmHg using a saline fluid column. **(b)** The ONH was sectioned coronally. Each section was imaged using fluorescence (FM) and polarized light microscopies (PLM) to visualize the vessels and collagen, respectively. Colors in the PLM image represent collagen fiber orientations. The LC region was defined based on the presence of collagen beams. **(c)** The vessel segmentations or "labels" were combined to create a 3D map of the vasculature. The vasculature covered a region larger than the LC. Vessels in the LC region were identified based on the LC segmentations.

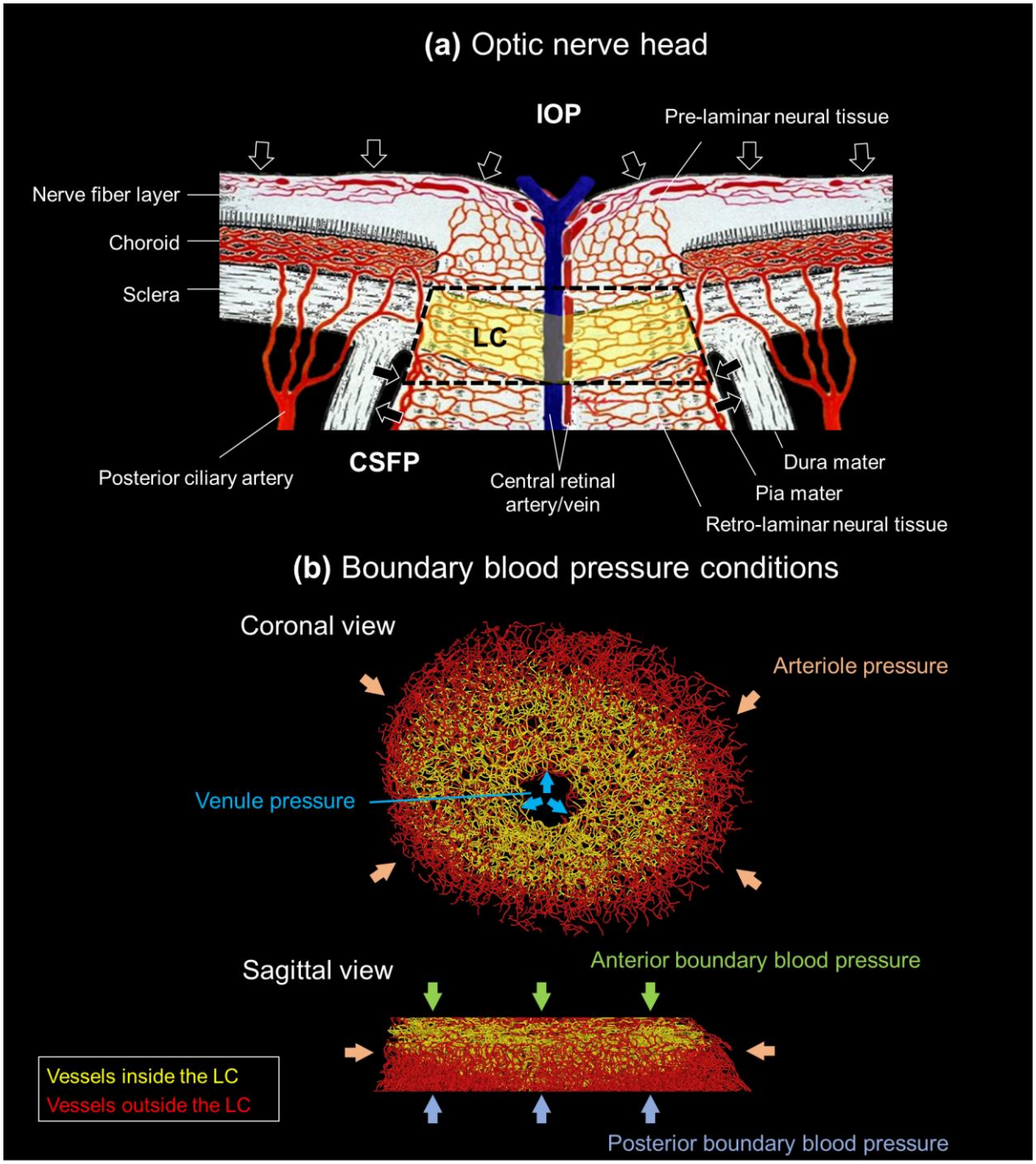

Figure 2. (a) A diagram of the ONH adapted from (Hayreh, 1969). Our model represents the vessels within the scleral canal, delimited at the periphery by the connective tissues of the sclera and/or pia mater, and at the center by the central retinal artery and vein. The anterior and posterior limits of the model are flat planes perpendicular to the central retinal artery and vein, located to ensure that the region modeled completely enclosed the LC. The black dashed lines represent the model boundaries. **(b)** Assignment of boundary blood pressure conditions. Four blood pressure conditions were assigned at the peripheral, central, anterior, and posterior boundaries of the model. The model periphery was assigned an arteriole pressure to represent blood flow from the circle of Zinn-Haller. The center was assigned a venule pressure to simulate blood drainage through the central retinal vein. The anterior and posterior boundaries were assigned blood pressures related to IOP and CSFP, respectively. See the main text for the rationale and details on how these pressures were assigned.

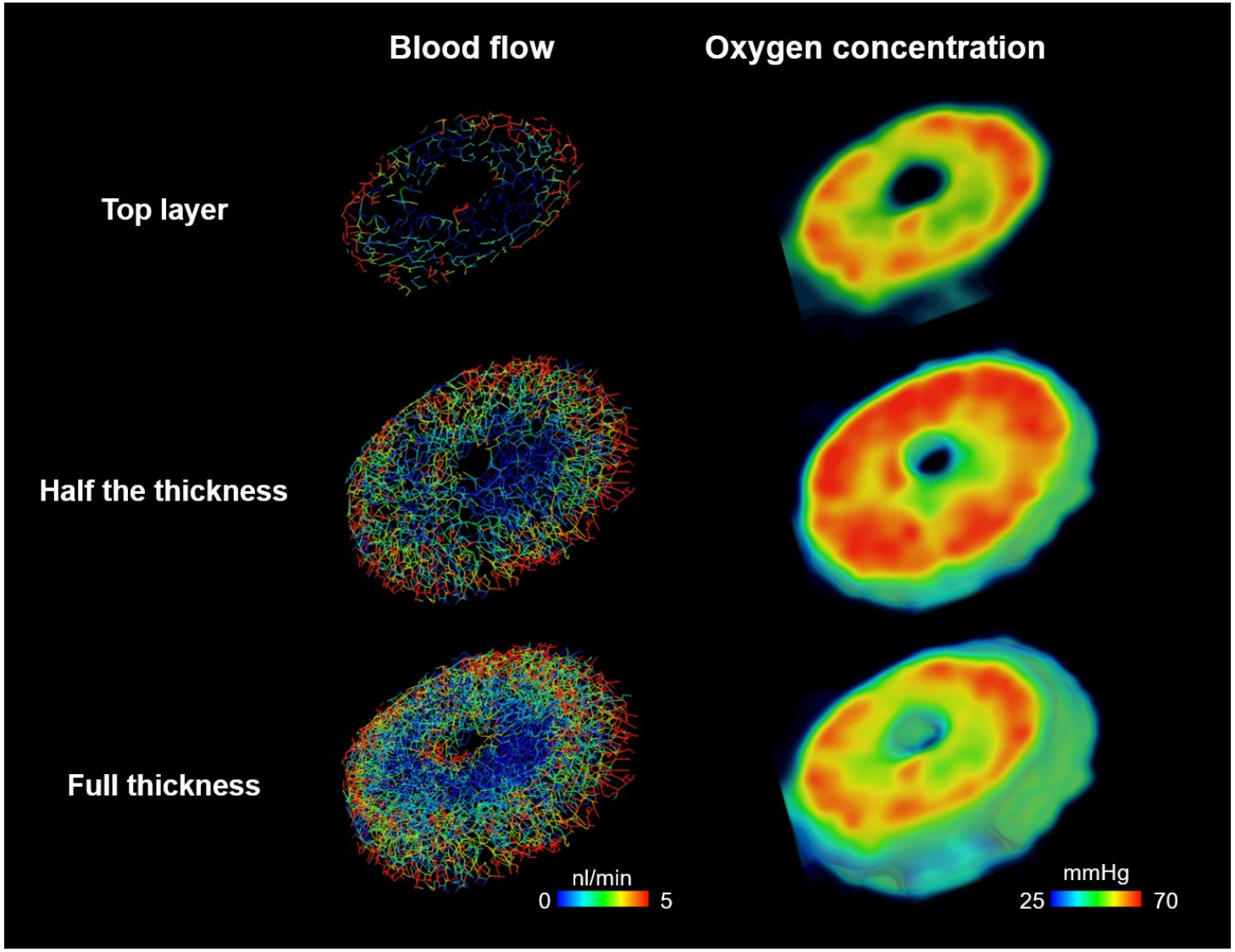

Figure 3. Lamina cribrosa vascular network colored by blood flow (left column) and contour plots of oxygen concentration in the neural tissues (right column). The plots are for a model with baseline values of all input parameters. Notice that there are similarities in the regional distribution of high/low blood flow and oxygen concentration, but there are also regions of disagreement.

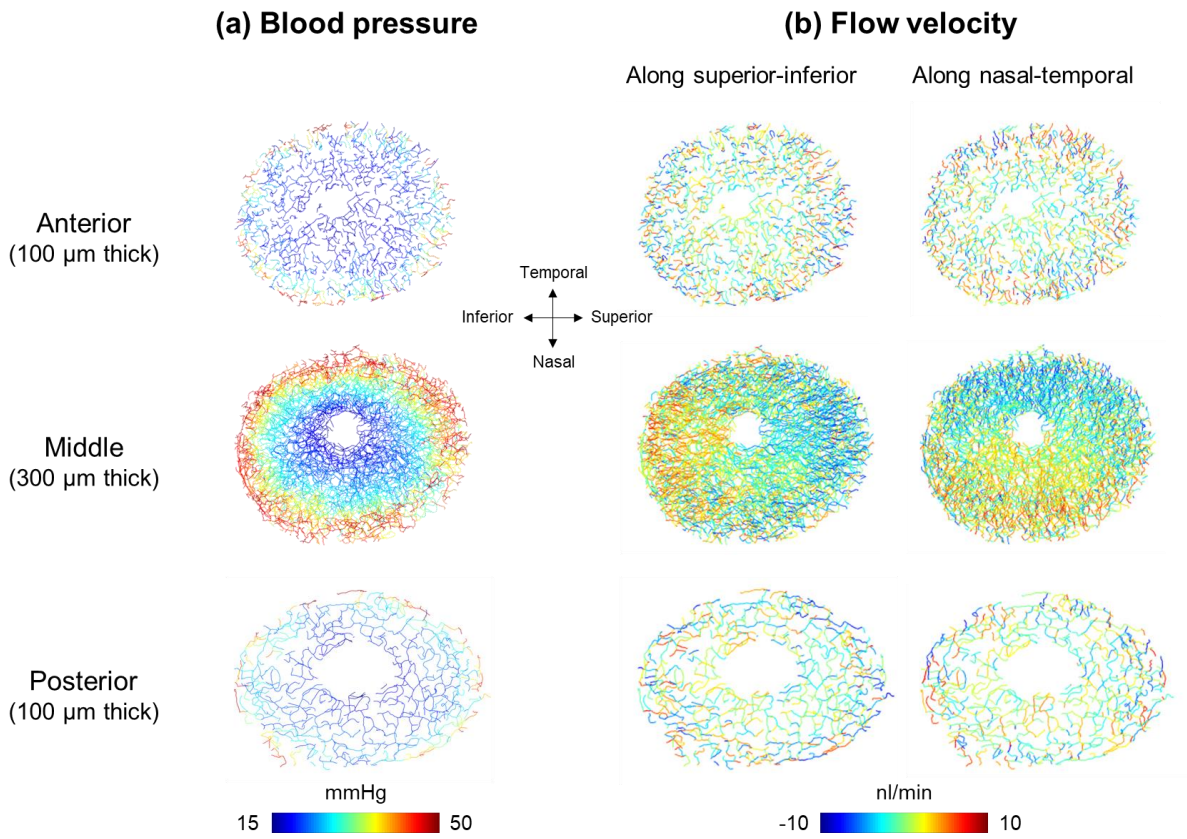

Figure 4. Distributions of **(a)** blood pressure and **(b)** flow velocity through the baseline model. The model was split into three layers: anterior (100 µm thick), middle (300 µm thick), and posterior (100 µm thick). The pressure was highest at the periphery, decreasing gradually towards the center, indicating that the blood flow was driven from the periphery to the center. This is further evidenced by the distributions of flow velocity.

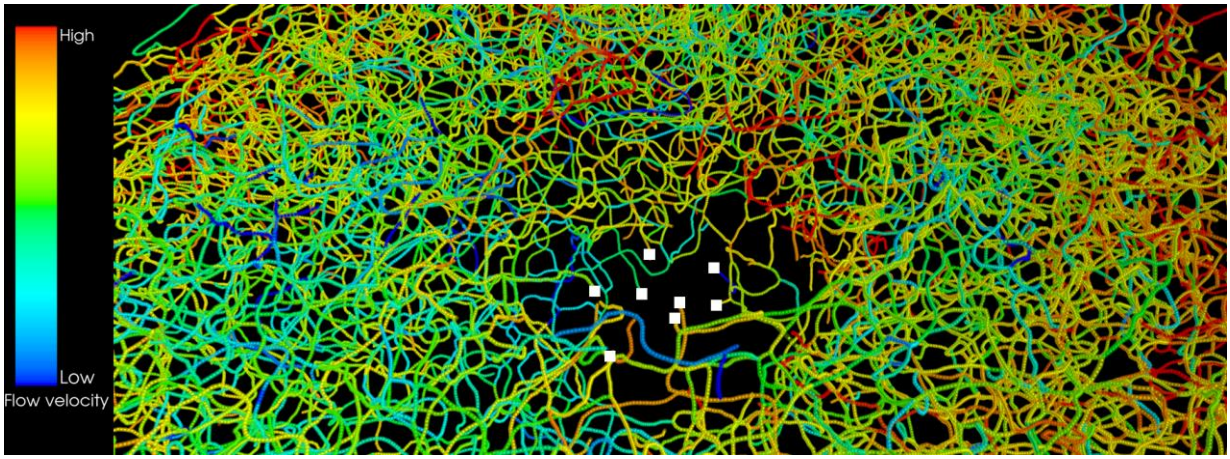

Figure 5. A still of the animation showing blood flow converging and draining via the central retinal vein opening (Video 2). Colors indicate blood flow rate. We used spheres to illustrate the movement of red blood cells. The density of spheres corresponds to hematocrit. The white squares indicate the points of outflow.

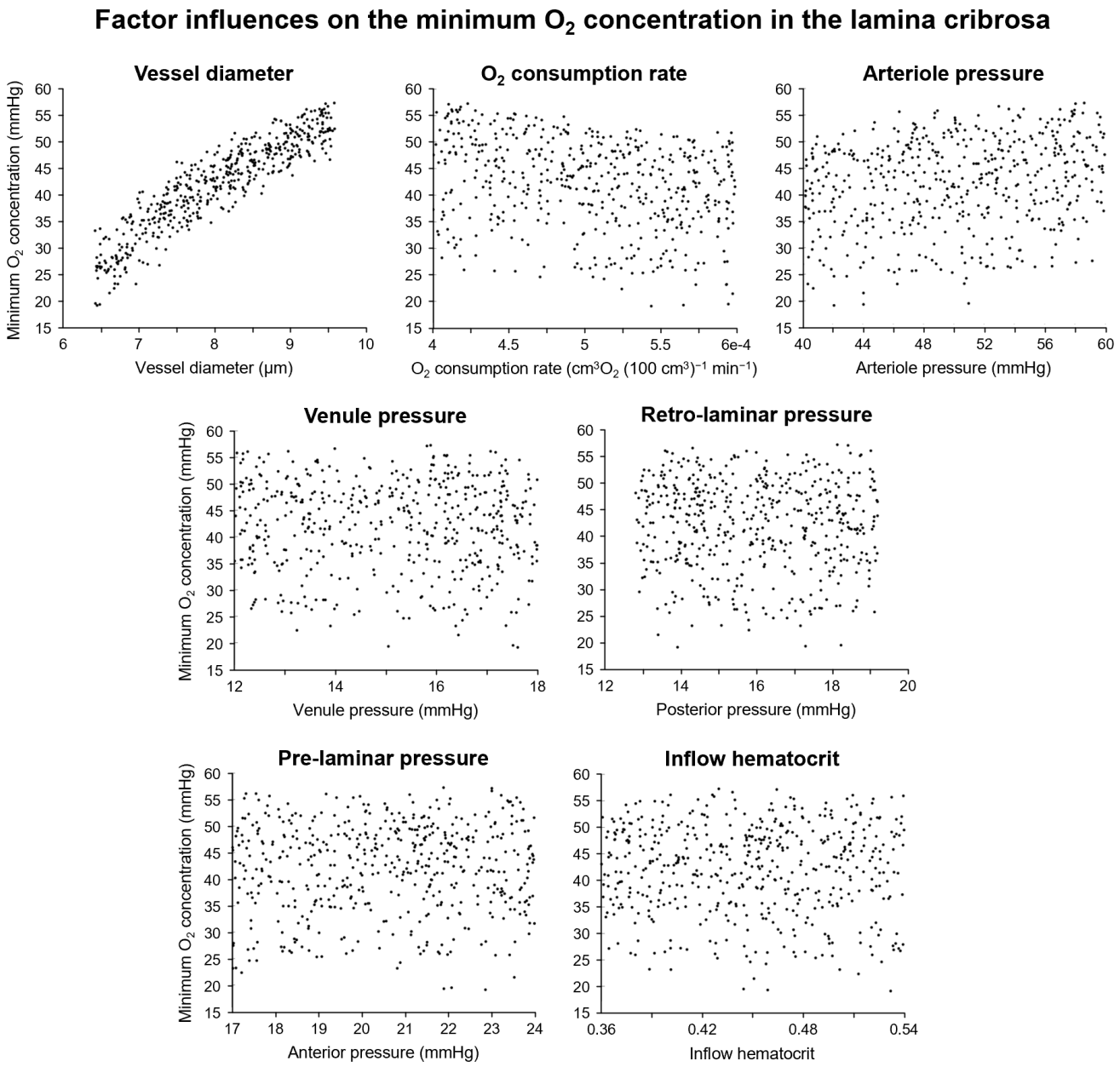

Figure 6. Scatter plots showing the factor influences on the minimum oxygen concentration in the lamina cribrosa. Each dot is one model. There was a clear association with the vessel diameter, O_2 consumption rate, and arteriole pressure, but the association with the other factors was not obvious.

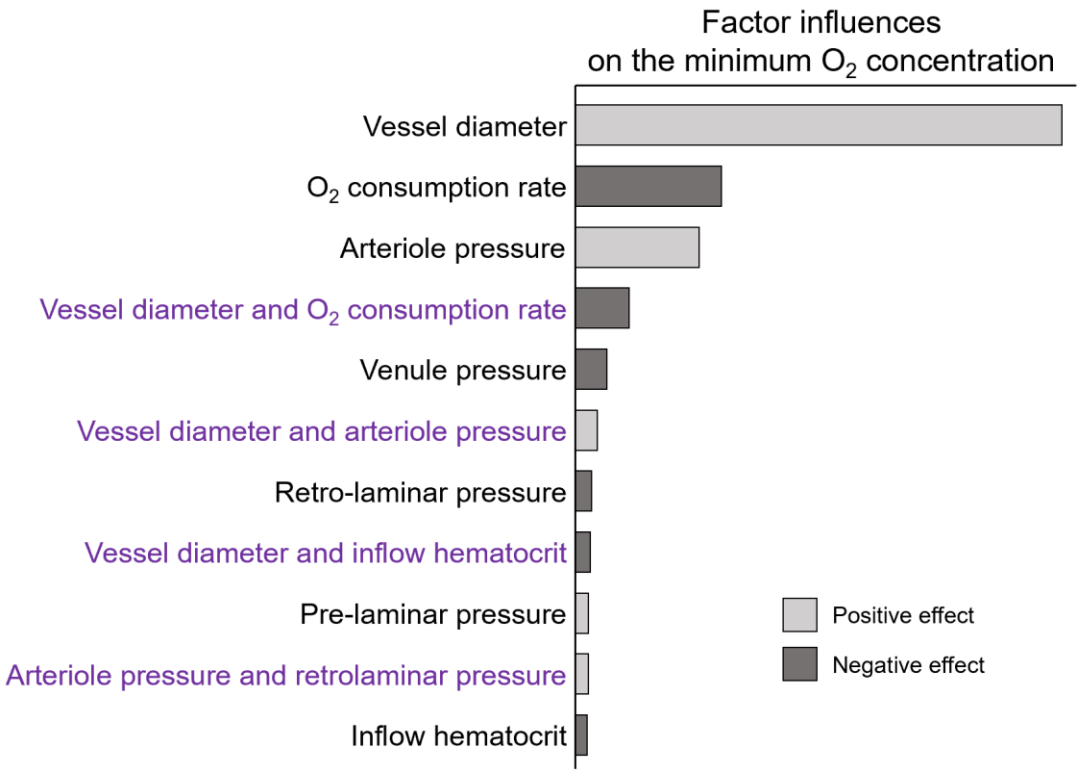

Figure 7. Bar chart showing the ranking of factors and interactions with respect to their influences on the minimum oxygen concentration in the lamina cribrosa, as determined by ANOVA. The vessel diameter, neural tissue oxygen consumption rate, and arteriole pressure were the three most influential factors, followed by the interactions between vessel diameter and arteriole pressure.

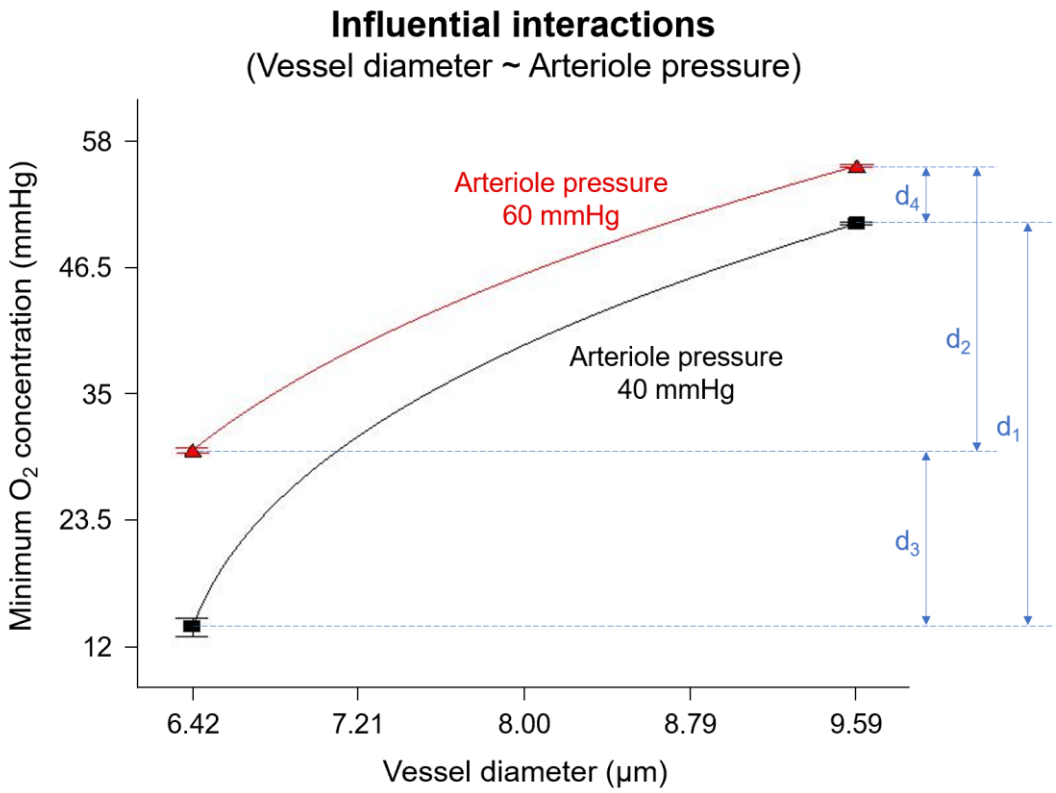

Figure 8. Effects of the interactions between vessel diameter and arteriole pressure on the minimum oxygen concentration in the lamina cribrosa. Nonparallel lines indicate that the effects of one factor depends on the other factor (*i.e.*, an interaction). Line endpoints are the mean responses for a given value of factors, whereas error bars depict the 95% least significant confidence interval. (Anderson and Whitcomb, 2017) Response range was chosen so as to make the interactions clearest. The interaction plot shows that the influence of the vessel diameter was more substantial when the arteriole pressure was low ($d_1 > d_2$). Similarly, the effect of arteriole pressure was more substantial when the vessel diameter was small ($d_3 > d_4$).

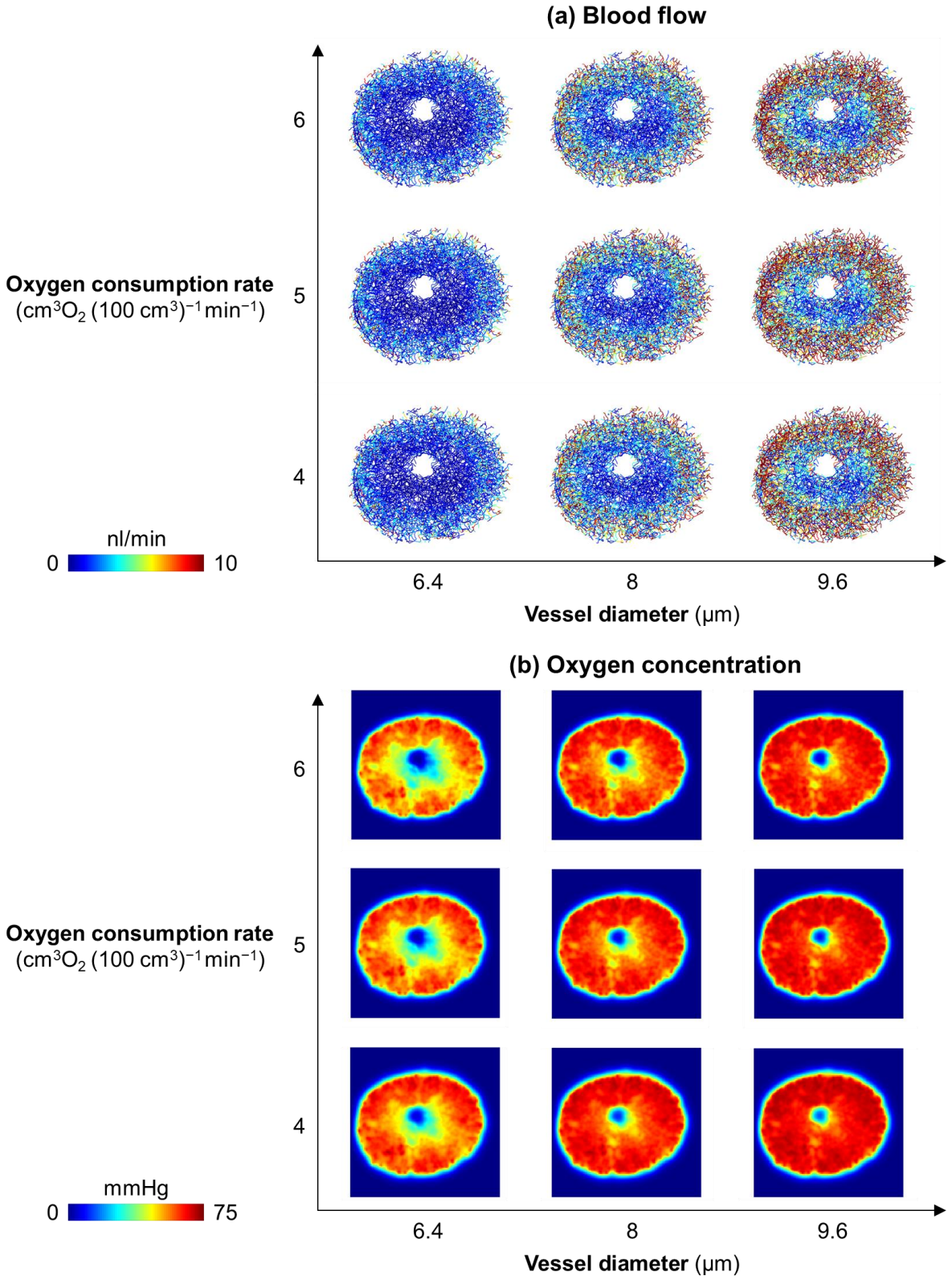

Figure 9. The distributions of **(a)** blood flow and **(b)** oxygen concentration of nine models with various combinations of vessel diameter and oxygen consumption rate. Shown are results in a 300 μm-thick slab through the middle of the region modeled. Oxygen concentration was higher at the periphery than at the center. Both vessel diameter and oxygen consumption rate affected oxygen concentration.